

Copyright © 1993, by the author(s).  
All rights reserved.

Permission to make digital or hard copies of all or part of this work for personal or classroom use is granted without fee provided that copies are not made or distributed for profit or commercial advantage and that copies bear this notice and the full citation on the first page. To copy otherwise, to republish, to post on servers or to redistribute to lists, requires prior specific permission.

**DIRECT AERIAL IMAGE MEASUREMENTS  
AT 248nm**

by

Charles H. Fields

Memorandum No. UCB/ERL M93/85

10 November 1993

*COVER PAGE*

**DIRECT AERIAL IMAGE MEASUREMENTS  
AT 248nm**

by

Charles H. Fields

Memorandum No. UCB/ERL M93/85

10 November 1993

**ELECTRONICS RESEARCH LABORATORY**

College of Engineering  
University of California, Berkeley  
94720

TITLE PAGE

**DIRECT AERIAL IMAGE MEASUREMENTS  
AT 248nm**

by

Charles H. Fields

Memorandum No. UCB/ERL M93/85

10 November 1993

**ELECTRONICS RESEARCH LABORATORY**

College of Engineering  
University of California, Berkeley  
94720

# **Direct Aerial Image Measurements at 248nm**

Charles H. Fields

Department of Electrical Engineering and Computer Sciences  
University of California, Berkeley

November 10, 1993.

## **Abstract**

A new method of testing high numerical aperture microlithographic lenses has recently been demonstrated. This method involves directly measuring the aerial image produced by the lens rather than using developed resist profiles or latent images produced in resist. Direct measurement of the aerial image eliminates any process variations associated with the resist processing and also removes the subjective nature of evaluating resist profiles.

We explore the use of amorphous silicon as an alternative to chrome for Deep UV photolithography masks. The primary advantage is that patterns may be dry etched. As masks feature sizes continue to shrink, this dry etch capability of Amorphous silicon can be a significant factor. Amorphous silicon has a further advantage of high absorbtivity over the 190-350nm region.

## Acknowledgments

I would like to thank my advisor, Professor William G. Oldham, for his encouragement and patient guidance throughout this project.

I thank Dr. William Partlo, formerly from GCA Tropel, for his work on the GCA XLS stepper which greatly facilitated the experiments done at GCA Tropel.

I wish to thank Richard J. Bojko at the National Nanofabrication Facility at Cornell University for all his help. Richard performed the e-beam patterning of the amorphous silicon wafers used to make the aerial image monitor artifacts.

We wish to gratefully acknowledge the support of the National Nanofabrication Facility and Knight Labs at Cornell University. We are grateful to the UC Berkeley Microfabrication Lab for the a-Si deposition work and to Alfred Wong for the TEMPEST analysis.

The assistance of my colleague, Anton Pfau, who had previously been involved in the project was essential for my understanding of the problem. Thanks also to Paul Haskel for his assistance in writing the C code for this project.

Thanks to Hamamatsu Sensor Corp., Maxim, and Analog Devices for the donation of the low-noise circuitry and photodiode sensors that made this research possible.

This research was supported by SRC/SEMATECH contract #91-MC-500.

## Table of Contents

Chapter 1: Introduction	4
Chapter 2: Amorphous Silicon	6
2.1 Introduction .....	6
2.2 Optical Properties of Amorphous Silicon.....	7
2.3 Fabrication.....	8
2.4 Simulation of Mask Images.....	9
2.5 Experimental Results.....	10
2.6 Conclusions.....	14
Chapter 3: 2-D Aerial Image Measurements	19
3.1 Introduction.....	19
3.2 Image Monitor Description.....	19
3.3 Experimental Results.....	20
3.4 Conclusions.....	22
References	31

# Chapter 1

## Introduction

The precise measurement of the aerial image of a lithography system is the key to the characterization of stepper performance. Image monitors which directly measure the aerial image incident on the wafer will allow the real time evaluation of the projected photolithography system without the costly and time consuming steps involved in evaluating images developed in resist. Direct image monitoring greatly improves accuracy by removing the resist stage entirely. The improved characterization speed and accuracy possible through aerial image monitoring will therefore improve the efficiency and overall quality of sub-micron lithography.

Previous image monitors used a one-dimensional scanning routine to monitor the intensity profile [14]. This process involves scanning a photodiode with a line grating pattern mask cover at the wafer under aerial images of the same pattern from the stepper reticle. The purpose of this research is to present a two-dimensional aerial images to monitor. This new image monitor uses arrays of pinholes in the mask to produce arrays of point light sources at the wafer plane as aerial image monitor. These images are monitored by scanning the photodiode detector under the images. The images pass through a cover placed on the diode which matches the image pattern. From the resulting intensity profile we can determine information on the characteristics of the stepper lens optics. Information that is available to us through this data includes: Lens aberrations, focus, distortion, coma, astigmatism, and light quality.

We have transferred this image monitoring technology to a commercial stepper. Based on materials received from GCA, we have completed the layout and fabrication of a new stage artifact to be used for the measurement of aerial images. This artifact was installed in a GCA stepper and used for the characterization of the

stepper performance. The image monitor test pattern consists of the basic 1-D GCA test pattern modified by the addition of 2-D sampling pinholes. Further details of this procedure will be covered in chapter 3.

Direct aerial image monitoring in quarter-micron lithography requires small sampling pinholes or slits. The ideal response of the intensity sampler would be an impulse function. This leads to the need for mask features of  $\sim 0.1\mu\text{m}$ . It is difficult to manufacture chromium masks with such feature sizes. As a result, in order to begin work on the design of an aerial image monitor, we will explore an alternate mask material for use in the deep UV region. It is to that topic that we now turn our attention.

## Chapter 2

### Amorphous Silicon for DUV Masks

#### *1. Introduction*

Deep UV steppers currently use reticle technology developed for longer wavelengths and larger feature sizes. Chromium shows particular weakness as an absorber both because of its limited absorbtivity and poor dry etchability. The relatively thick films ( $\sim\lambda/4$  to  $\lambda/2$ ) and poor wall angles and edge slopes in wet etch technology, limit the minimum useful feature size. Partial transmittance at these feature edges leads to image corruption at the wafer. These factors make the manufacturing of 4X and 5X masks for quarter micron lithography very challenging and the making of 1X masks truly formidable.

We propose the use of amorphous silicon as a preferred material over chrome for Deep UV masks. The primary advantage is that patterns may be dry etched. The near vertical sidewalls achieved through dry etching the amorphous silicon means that the thickness remains constant until the very edge of the mask feature. Amorphous silicon has a further advantage of higher absorbtivity over the 190-350nm region.

We have characterized the reflectivity and absorption of amorphous silicon, polysilicon, and chrome in the Deep UV range from 190nm to 360nm. The optical properties of amorphous and polysilicon are very similar, but the superior homogeneity of amorphous silicon for etching makes it the preferred form. The absorbtivity of silicon exceeds that of chrome in this region (by  $\sim 20\%$ ); consequently a 700Å film is adequate to insure transmission of less than .01%.

We have examined both optical and e-beam mask making processes. The amorphous silicon is deposited on quartz blanks by means of LPCVD. After

removing the backside film, the pattern is transferred to the silicon using e-beam or optical exposure. The pattern is then developed by a dry plasma etch. We have fabricated an experimental mask set at the National Nanofabrication Facility at Cornell with feature sizes down to 0.2 $\mu\text{m}$ .

The thickness of such chrome masks for sub-quarter micron lithography would exceed the width of the slits in line space patterns and therefore reduce the acceptance angle of the mask. A material with a higher extinction coefficient would not suffer from this restriction. The higher acceptance angles would facilitate the use of these masks with higher NA optical systems.

## *2. Optical Properties of Amorphous Silicon*

Structural disorder and the hydrogen in a-Si:H make its optical properties quite different than that of crystalline silicon in the visible and IR spectrum [6]. The optical band gap of crystalline silicon is about 1.1 eV while the band gap of amorphous silicon is typically about 1.7 eV. The region of interest for this paper is the Deep UV range. In this region the optical properties of the two types of silicon are more closely related.

Amorphous silicon is also known to demonstrate higher optical absorption at photon energies above 1.7 eV. However, all of the sources under investigation here are above 3.4 eV. Since the incident energy in all cases is well above the bandgap, the absorption properties of amorphous silicon are close to those of crystalline silicon. The material is similar to a metal and its properties largely unrelated to near-band-edge electron states.

The optical properties of amorphous silicon in the visible spectrum are greatly dependent upon deposition conditions. Factors such as Hydrogen content of the process gas can have the affect of modifying the bandgap [8]. In fact is has been shown [2] that a 10 atomic percent of hydrogen in the a-Si increases the optical gap from about 1.5eV to 1.7eV. Quantization effects cause further bandgap modulation in ultrathin amorphous silicon layers [9] [10]. This has the overall affect of changing the index of refraction as well as the optical absorption coefficient. Thin films of amorphous silicon that might be used in masks in the visible spectrum would be affected by both types of modulation. However, these factors should play little role in the DUV; the optical properties of amorphous are assumed to be similar to those of single crystal silicon.

### *3. Fabrication*

Amorphous silicon was deposited onto silicon substrate wafers and quartz blanks by means of LPCVD at 580 deg. C. The deposition process used was designed for a bulk deposition rate of 64A/min. for process times of over 30 minutes. The growth rate was first characterized by deposition on SiO<sub>2</sub> covered silicon wafers. A 1000A SiO<sub>2</sub> layer was grown on the silicon substrate wafers as a base on which to deposit the amorphous silicon. The film thickness of these monitor wafers was accurately measured by ellipsometry on a Nanometrics NANO-DUV thin-film measurement system. These monitor wafers were used to characterize the process and to determine specific process times for different deposition thicknesses. Figure 2.1 illustrates the reproducibility of the LPCVD process.

#### 4. Simulation of Mask Images

Simulations were done to investigate the effect of undercutting on the aerial image. We used the U.C. Berkeley program TEMPEST which simulates the EM wave incident at the wafer given the parameters of illumination and mask material.

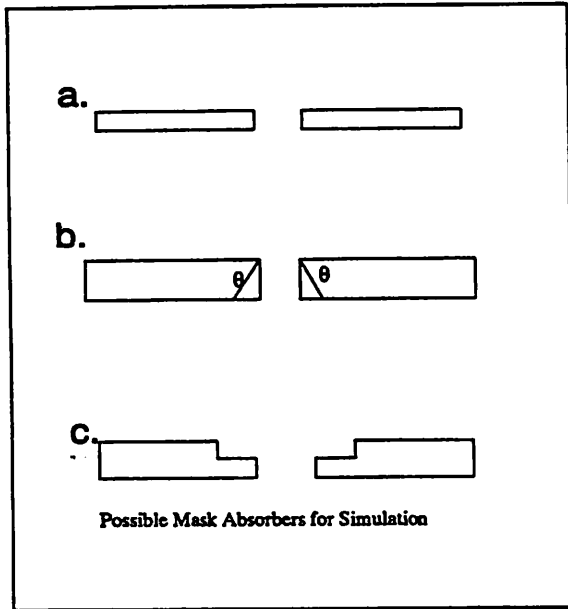


Figure 2.2 shows simulations of the intensity profile from a 2.5 micron feature on a 5X chrome mask. The figures in the inset show the mask edge profiles used for the chromium mask in the simulations illustrating the sloped sidewalls for varying degrees of theta ( $\theta$ ). Profile a is the edge profile of an a-Si mask feature patterned with a purely anisotropic etch. The simulations address the patterning of a 0.25  $\mu\text{m}$  contact hole on a NA=0.5 sigma=0.7 optical projection system with an

800A Cr mask. These simulations show that the image intensity degradation that results from the partial transmittance of the pattern edges is not significant for reduction stepper systems.

Another possible use of amorphous silicon is the absorber for partially transmittance phase-shifting masks for DUV lithography. Edge-rimmed phase shift masks use rims around the feature edges that are thinner than the bulk thickness as in profile c. The thickness of the material at the rims is chosen such that a 180 deg. phase shift is obtained as the source intensity passes through the edge. This phase shift has the effect of canceling out the incident intensity at the edge and produces a null.

The process of producing such a phase shift masks requires a secondary etch step to define the edge rims. The etch must be able to both produce nearly vertical edges but also not completely etch the entire surface. The etch must leave the exact amount of mask material to produce a 180 deg. phase shift. As described earlier, the simple dry used in a-Si masks is highly desirable for manufacturability of such structures.

## ***5. Experimental Results***

### ***A. Measurement of Absorption Coefficients***

In our experiments, we attempted to evaluate the optical properties of thin films of amorphous silicon and chrome. We wish to compare the absorption coefficient of these two materials. A requirement of masks is that they either absorb the incident energy or reflect it so as to produce a differential intensity profile at the wafer plane.

The amorphous silicon deposition process described earlier deposited the silicon uniformly on both sides of the quartz blanks. In the mask application, one side was etched off; however, for material characterization the second layer proved useful. Since the optical properties of a-Si is known to be strongly dependent upon deposition conditions, double sided and single sided-wafers both from the same batch run provides a means of verifying the accuracy of the absorption coefficients. Single-sided wafers were made by coating one side of double-sided wafer with resist and selectively removing the amorphous silicon from the back side.

We measured the optical absorbance and transmittance of the test wafers with the use of an HP-DAS Diode Array Spectrometer. The optical properties of both single and double sided amorphous silicon wafers and chrome were measured on the DAS for wavelengths in the Deep UV range. In this range, four specific

wavelengths are significant for DUV Lithography: 365nm (i-line), 248nm, 213nm, and 193nm.

Figures 2.3 show the raw data results of the tests. The factory recommended range of operation for the HP-DAS used in these measurements is for absorbance values from 0 to 3. Indeed from figure 2.3 the increase in noise is evident in all the absorbance measurements above 3. Although there is a substantial amount of noise in measurement for the chrome mask (top line in fig. 2.3), the data will suffice to demonstrate the general trend in the spectral response. Chromium demonstrated nearly linear spectral absorbance across the band.

Amorphous silicon ( $\alpha$ -Si) test wafers were tested at several thin film thicknesses. Figure 2.3 shows similar spectral shaping of the absorbance of the  $\alpha$ -Si films at 218A, 422A, and 436A (the lower three curves). Note the slight increase in noise of the 436A wafer at its peak absorbance ( $\sim$ 3). This increase in noise is expected as mentioned previously. While the data shows similar spectral shaping for the first three wafers, a distinct difference is noted in the 490A test wafer. This test wafer was N2 annealed at 750 deg. C. for 20 minutes following the deposition. It is known that annealing at temperatures above  $\sim$ 600deg. C. will have the affect of reforming the crystalline structure and the resultant film is therefore polycrystalline [1],[3]. The response of this film shows a much sharper absorption edge around 350nm than the other three  $\alpha$ -Si films. This is expected from theory since the bandgap of the polycrystalline film is more well defined than the gap for  $\alpha$ -Si. The tail states in amorphous silicon lead to a less defined optical gap and therefore a less steep roll-off in absorbance at these wavelengths [2]. Despite the differences at longer wavelengths, the poly-silicon displays similar response in the DUV region below 300nm as expected.

Figure 2.4 plots absorption coefficient vs. wavelength. This figure as well as all future spectral response plots are taken from the raw absorbance data. The absorbance value was taken at the wavelengths of interest only in an attempt to reduce the data. Then calculations of the absorption coefficient were made taking secondary surface reflections into account.

Figure 2.4 shows the dependence of the  $\alpha$ -Si absorption coefficient on run to run process variations. The 218A and 436A wafers were deposited during the same process run. The difference being that the thinner film was single-sided and the thicker one was double sided. The 422A wafers were single sided. Although there were accompanying 844A wafers, the absorbance was above 4 and the DAS saturates at absorbance values around 4. Therefore accurate information at the thicker film ranges was not available. The 490A wafers were each done on separate runs and one of them had the additional annealing step mentioned earlier. The data from figure 2.4 shows that the optical properties of the resulting silicon films were consistent within the same run but differed slightly from run to run. This figure confirms that the optical properties of  $\alpha$ -Si are indeed very dependent upon deposition process conditions such as temperature and gas flow. The dependence appears such that minor variations in these parameters from run to run affect the optical properties of the resulting films.

Figure 2.5 shows the results of the absorption coefficient measurements of a three 900A chrome masks. The masks used were anti-reflective chrome on quartz masks from Hoya. The data for the chromium masks is very consistent.

## *B. Applications for Deep UV Lithography*

The GCA XLS stepper uses a technique for determining best focus that involves an insitu detector known as a stage artifact. This sensor is made up of a photo diode and a mask cover consisting of arrays of 0.8 micron lines. These lines at the mask plane are scanned against identical line patterns at the wafer plane. The resulting intensity profile gives information concerning best focus of the system. The ability to produce a mask cover with thinner lines would lead to better resolution in determining best focus. The currently installed mask, with 0.8 $\mu$ m features, is made of chrome. Fabrication of a mask with smaller dimensions is nearly impossible with chrome.

In Cooperation with the National Nanofabrication Facility (NNF), we have manufactured such a stage artifact in amorphous silicon. The a-Si was deposited under the process described earlier to a thickness of 890 Angstroms. An array of 0.2 $\mu$ m lines and dots were patterned in the silicon by e-beam processing and plasma etching.

Figures 2.6 and 2.7 show SEM photographs of the line and pinhole patterns of the a-Si stage artifact mask patterned at the NNF. The photos show good resolution of line patterns as well as nearly square edges on the 0.2 $\mu$ m pinholes. These photos are examples of the high pattern resolution available through the use of amorphous silicon, e-beam exposure, and anisotropic plasma etching. Figures 2.8 and 2.9 are SEM photos of the modified stage artifact showing both the original 0.8 $\mu$ m lines and the new 0.2 $\mu$ m sampling slits.

One of these stage artifact mask covers was installed on an XLS stepper and used to characterize best focus. The result of this new finer line artifact was greater resolution of focus. The enhanced sensitivity of the GCA setup procedure using the artifact is described elsewhere [12].

## **6. Conclusions**

The four primary wavelengths for DUV Lithography are: 365nm (i-line), 248nm, 213nm, and 193nm. At these wavelengths amorphous silicon shows a higher absorption coefficient than chromium. This leads to the ability to manufacture masks with reduced thicknesses and therefore better aspect ratios. The improved aspect ratios lead to higher acceptance angles for the mask features. Amorphous Silicon has the further advantage that it may be patterned by dry etching. This provides the ability to produce smaller mask pattern features with improved sidewall angles. While the absorption spectrum for polycrystalline silicon is similar to that of  $\alpha$ -Si, the superior homogeneity of the  $\alpha$ -Si makes it the preferred form of silicon for dry etching. Amorphous silicon provides smoother edges during the pattern etch. Polycrystalline silicon suffers from grain boundary roughness when etching such small line dimensions.

Figure 2.10 shows the average absorption coefficient for the materials tested. From the data we note that at the primary wavelengths of interest, thin films of amorphous silicon shows a nearly equal or higher absorption coefficient to that of Chromium. Thus thin films of amorphous silicon (600A-700A) used in masks are expected to have <.01% transmission with high confidence.

# Amorphous Silicon Dep. Rate LPCVD 580C 100sccm Si:H4

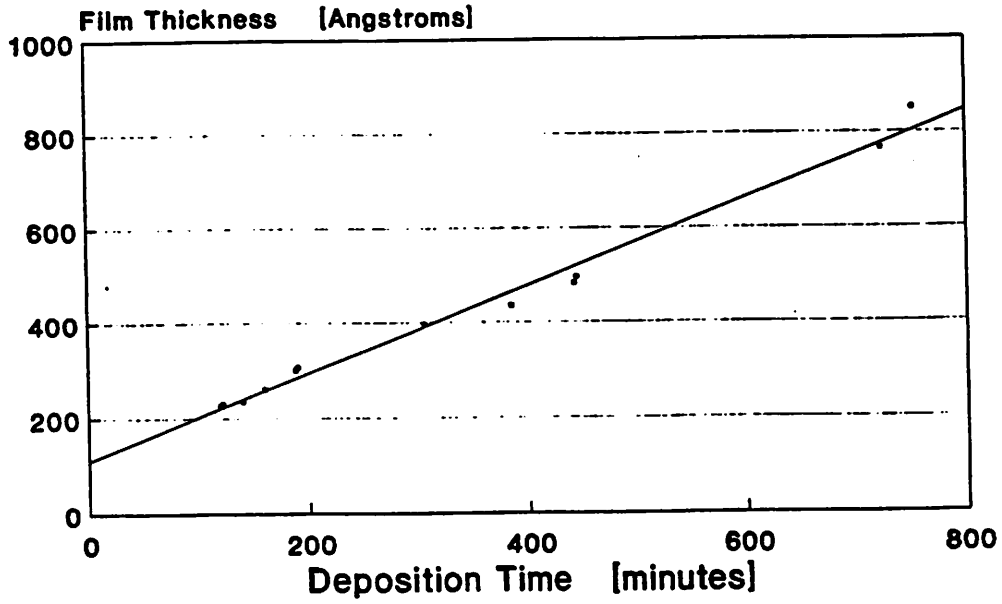


Figure 2.1 Amorphous Silicon Deposition Rate

## 5X Chrome Mask Edge Effects (TE)

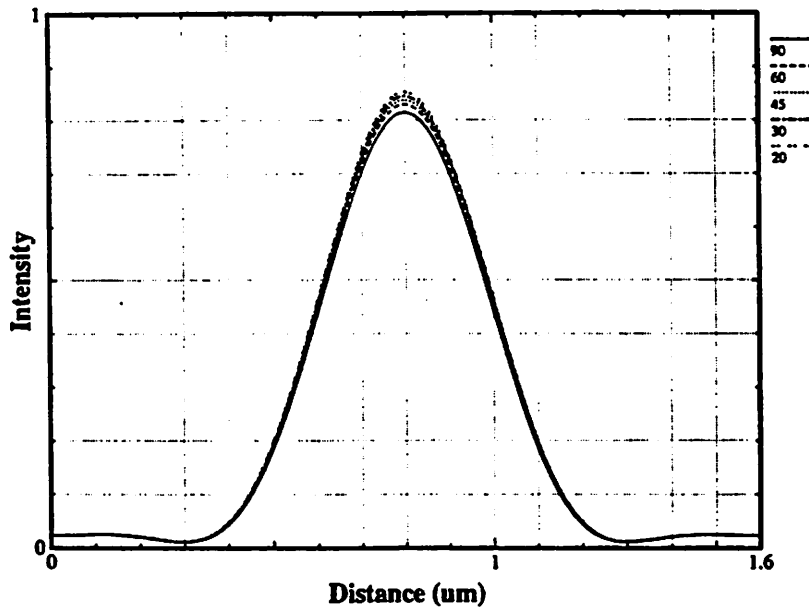


Figure 2.2  
Tempest Simulation of 0.25 $\mu$ m feature for varying mask edge angle (see inset  
in chapter two on page 9).

### Absorbance vs. Wavelength

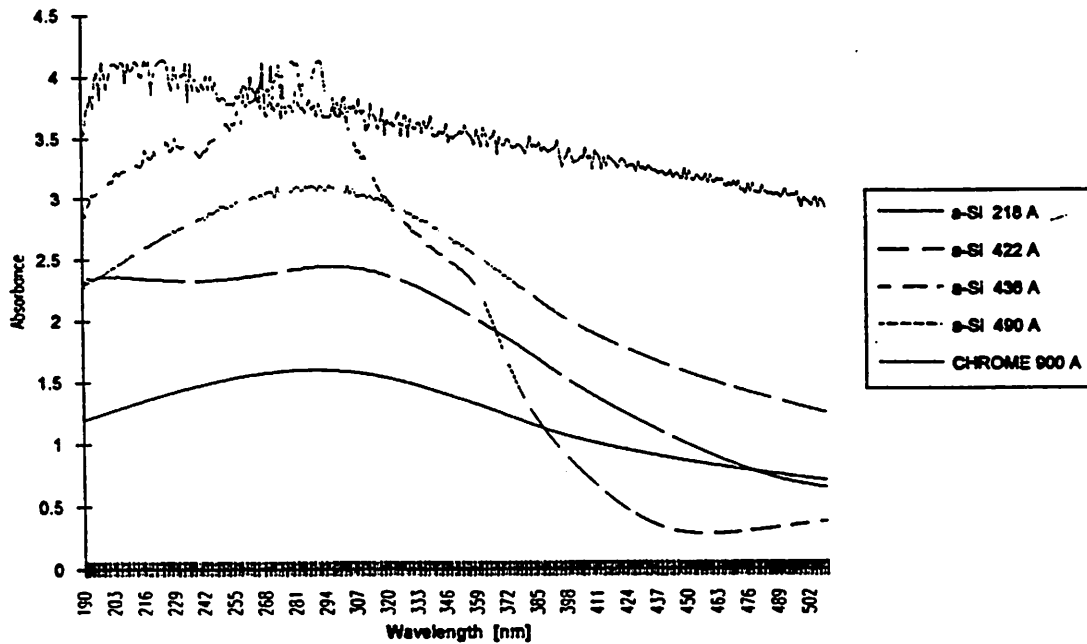


Figure 2.3  
Absorbance vs. Wavelength for varying thickness of a-Si and Chrome

### Amorphous Silicon Absorption Coefficients

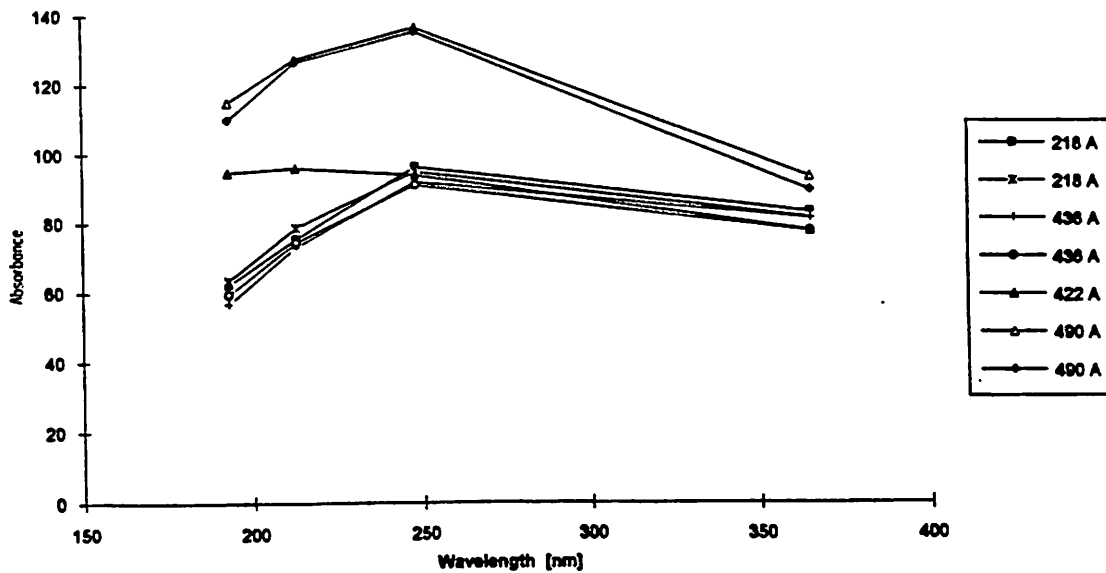


Figure 2.4  
Absorbance vs. Wavelength for Amorphous Silicon

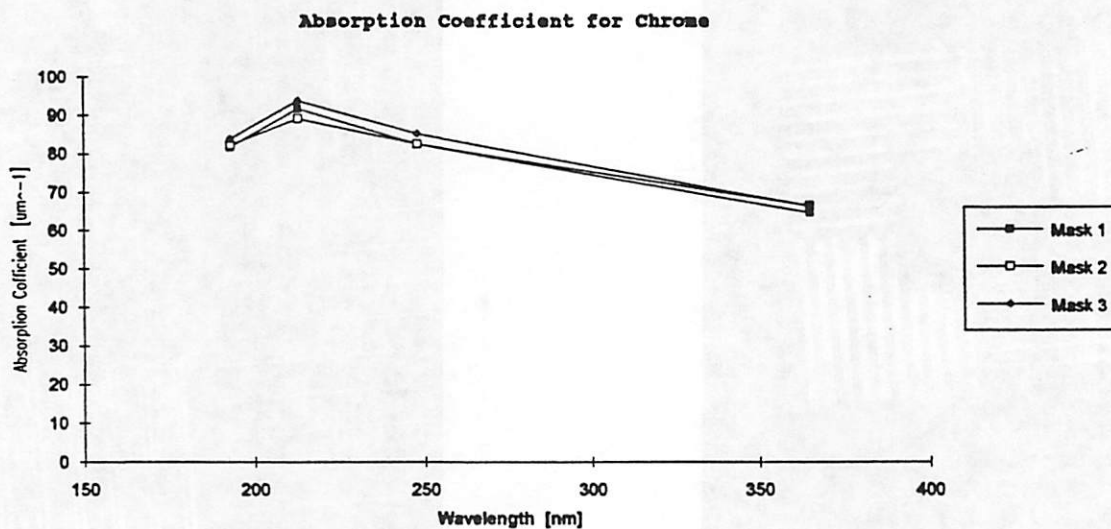


Figure 2.5  
Absorbance vs. Wavelength for 3 Chrome Masks

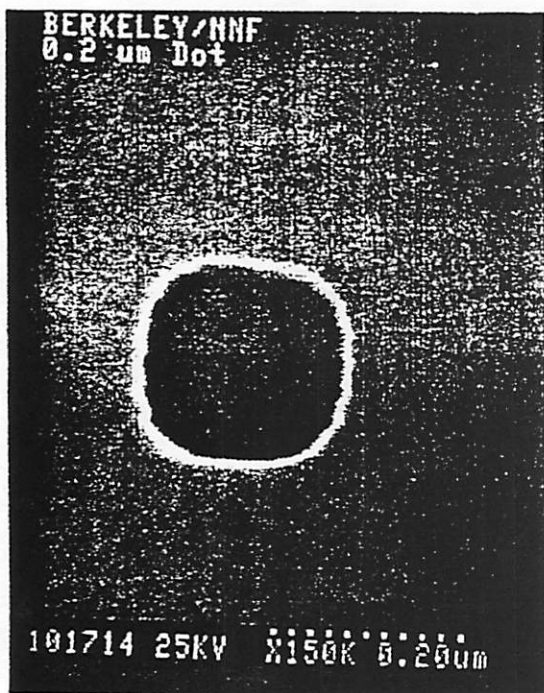


Figure 2.6  
SEM Image of 0.2 $\mu$ m Pinhole in  
Amorphous Silicon

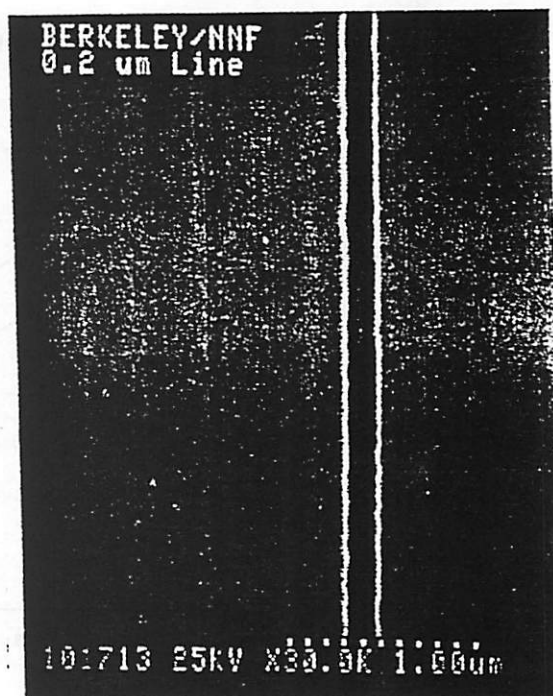


Figure 2.7  
SEM Image of 0.2 $\mu$ m Line in  
Amorphous Silicon

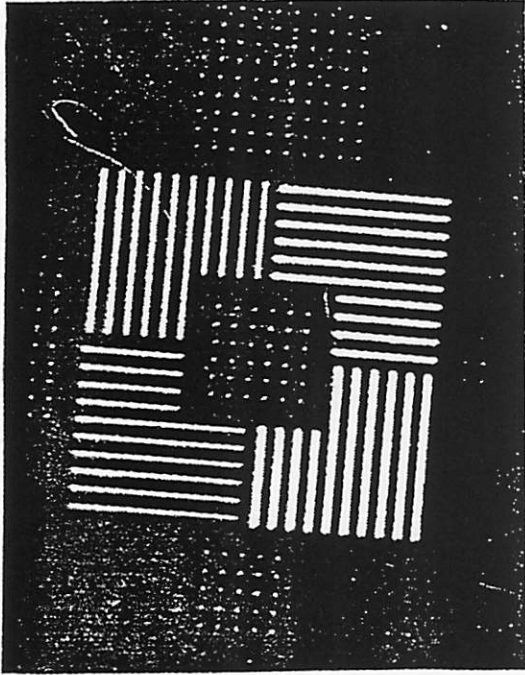


Figure 2.8

SEM Images of Aerial Image Monitor Artifact

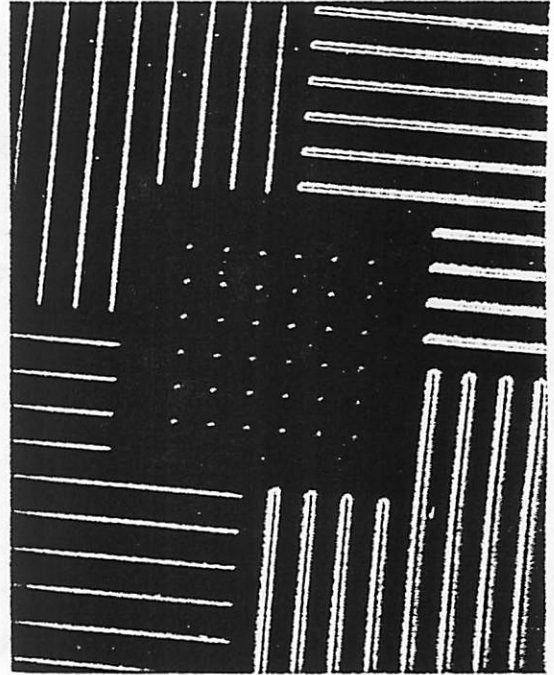


Figure 2.9

Average Absorption Coefficients of a-Si & Cr

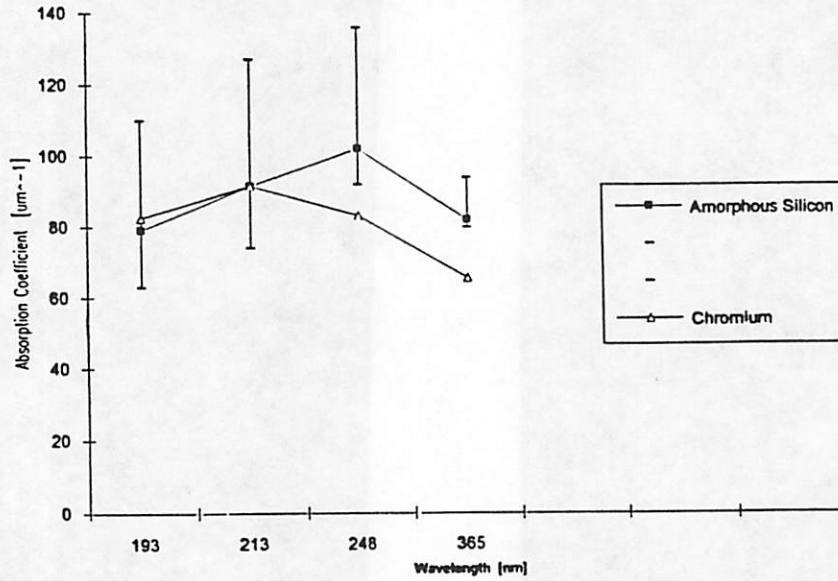


Figure 2.10

Average Absorption Coefficients of Amorphous Silicon and Chromium vs. Wavelength in the Deep UV Region.

## Chapter 3

### ***1. Introduction***

A fully assembled microlithography lens is traditionally tested in two ways. The first method is to measure the wave front aberrations using a transmissive interferometer. Transmission interferometry is critical to adjusting the spacing and positioning of each lens element and subgroup. To quantify the final performance of a lens, a second method is used. Producing exposures in photoresist and measuring the developed resist profiles in a scanning electron microscope (SEM) is the method used for quantifying the final lens performance. These SEM verified exposures have several drawbacks. First, the time needed to make all of the required SEM measurements is very long; approximately two days. In addition to the time consuming nature, the photoresist exposure measurement method is subject to changes in the photoresist process and differences in SEM operator performance.

By measuring the aerial image directly, variations due to the photoresist process and SEM linewidth measurements are eliminated. In a separate paper we have shown that a simpler 1-D version of the same monitor can be used to rapidly characterize a stepper lens *in-situ* [12]. The technique described in this paper uses measurements of the transmitted energy through a set of small sampling pinholes with a 2-dimensional scanning procedure. This system has been implemented on a 0.53 NA lens operating with a 248nm KrF laser source. The microlithographic system was designed for imaging 0.35 $\mu\text{m}$  features.

### ***2. Image Monitor Description***

The aerial image monitor used for these experiments consists of an artifact cover with a series of 2-D scanning pinholes placed over a photodetector. The artifact itself was manufactured by depositing 800Å of amorphous silicon onto

quartz blanks. The  $0.2\mu\text{m}$  sampling pinholes were patterned in the amorphous silicon by electron beam lithography as described in chapter 2. The artifact consists of a  $10\times 10$  array of these pinhole patterns on a  $6.0\mu\text{m}$  pitch [13].

Figure 3.1 illustrates the method of aerial image monitoring. The technique for the measurement is to project an aerial image onto the artifact sensor. The stage is then scanned in one direction to obtain a one-dimensional image intensity profile "slice". The stage is then stepped in the other direction and another scan is performed. After several repetitions of this step and scan procedure, a 2-D image is obtained by piecing together all of the 1-D "slices". Fig. 3.2 shows the result of using this technique to obtain a 2-D aerial image intensity plot of a  $0.35\mu\text{m}$  pinhole.

### ***3. Experimental Results***

The aerial images scanned in this experiment were produced from conventional binary DUV masks. The resulting image of three types of patterns are presented here: Contact holes, nested elbow arrays, and isolated line patterns. The resulting measurements are then compared with numerical simulation of the image produced from SPLAT.

The first image is a  $0.35\mu\text{m}$  contact hole. The data from figure 3.2 can also be plotted as a contour plot. Fig. 3.3 shows the 3-D plot of the direct measured aerial image while Fig. 3.4 shows the result of the numerical simulation. Comparison of the two shows good correlation between the measured and simulated images with respect to the full width half maximum (FWHM) value as well as the peak contrast. The contrast for a perfect lens with no aberrations would be 100% and indeed the simulated image shows a contrast of 99.99% The contrast of the measured image is seen to be 84%. Most of this reduction in measured contrast can be accounted for by the width of the pinhole used for the sampling. Convolution of a 0.2 micron pinhole with the simulated  $0.35\mu\text{m}$  aerial image reduces the peak

contrast to 88%. The remaining 4% difference between measured and simulated is likely due to the finite bandwidth of the laser source (1.4pm) [12].

The second image scanned was that of a nested elbow array pattern. This pattern consist of three 0.5 $\mu$ m linewidth elbows on a 0.5 $\mu$ m pitch. Figure 3.5 shows the intensity plot of the aerial image scan. Figs. 3.6 and 3.7 show the result of the measured and simulated images of this pattern respectively. The lower half of the outermost elbow is missing from the measured plot due to the limitation of the stage travel in the fine scan. For this reason, the simulation was done to compare only the available scanned data. Once again we see that the measured data fit the simulation very well. The FWHM linewidth corresponds to the 0.5 $\mu$ m linewidth with 200 counts on the measured data plot corresponding to 1.0 $\mu$ m. Once again we see a peak contrast of ~84%.

The final image scanned was that of an isolated line pattern. The pattern consists of three lines that are 0.35 $\mu$ m wide and on a 0.35 $\mu$ m pitch. The two lines on the either end are 1.0 $\mu$ m long while the middle line is 1.5 $\mu$ m in length. This effectively gives us an isolated line.

Fig. 3.8 is an intensity plot of the directly measured aerial image and Fig. 3.9 is the contour plot of the image. While the linewidth of the measured image appears to be correct, the measured contrast of this image is only about 60%. Comparisons were done with the measured image and the simulated images of the isolated line pattern with differing focus values. It appears that at the time this image was measured, the feature was about 0.5 $\mu$ m out of focus. Figs. 3.10 and 3.11 show the simulations results for zero and 0.5 $\mu$ m of defocus respectively. We know that the in-focus contrast for 0.35 $\mu$ m features is high from the 1-D scans done on the same lens [12]. No special care was taken during the image measurements to insure that the images were at best focus. On the contrary, this provides a good example of the ability of this aerial image monitor to quantify the performance of the stepper.

#### **4. Conclusions**

Previous 1-D Aerial Image Measurements have demonstrated the ability to quantify all of the primary lens aberrations. This is accomplished with lines scans by measuring contrast through focus. The details of this technique are described elsewhere. By varying such parameters as the partial coherence and performing multiple scans, we are able to obtain the quantitative information concerning the lens aberrations. An advantage of direct 2-D Aerial Image Monitoring is its ability to directly obtain information on lens aberrations with a single scan. Figures 3.12 through 3.16 illustrate this point. These figures are SPLAT simulations of our original 0.35 $\mu$ m square contact but this time with differing lens aberrations. As can be seen from the figures, each type of aberration produces a distinct aerial image which is easily distinguishable from the normal unaberrated image (see fig. 3.4).

The ability to directly measure lens and stepper performance using aerial image measurements has been demonstrated on a commercial DUV stepper. This technique offers the advantages of speed and repeatability over the present method of SEM evaluation. This technique also offers the ability to directly quantify many lens aberrations such as astigmatism, spherical aberrations, and field curvature.

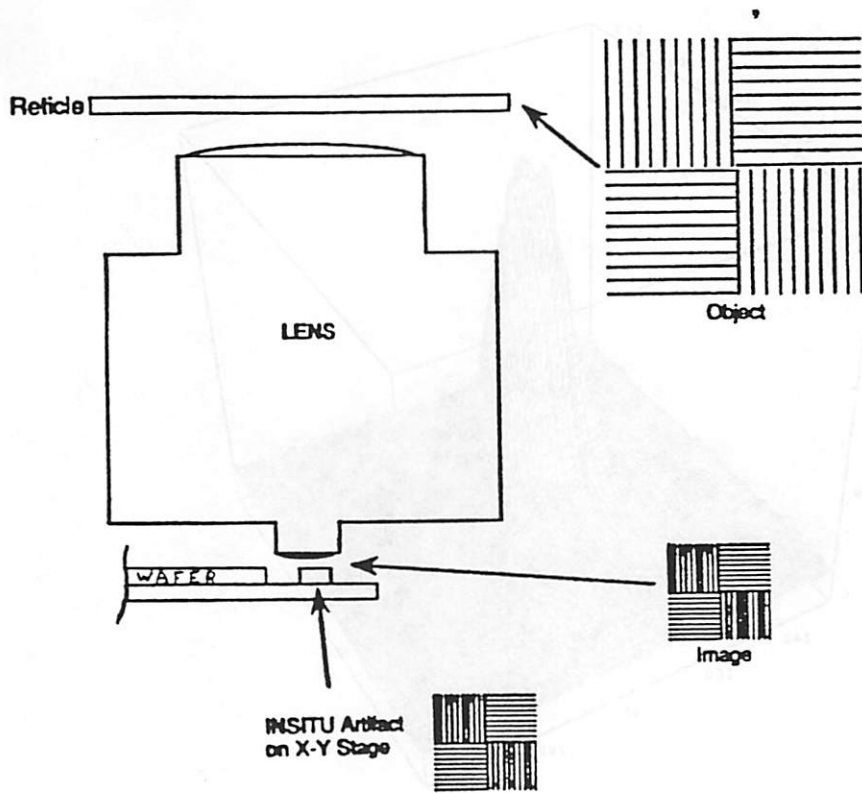


Figure 3.1  
Aerial Image Monitor System

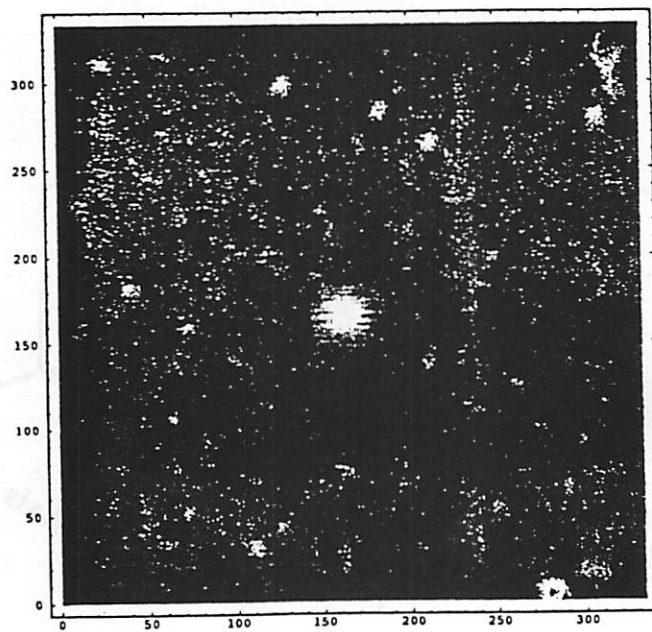


Figure 3.2  
Intensity Plot of 0.35μm Contact

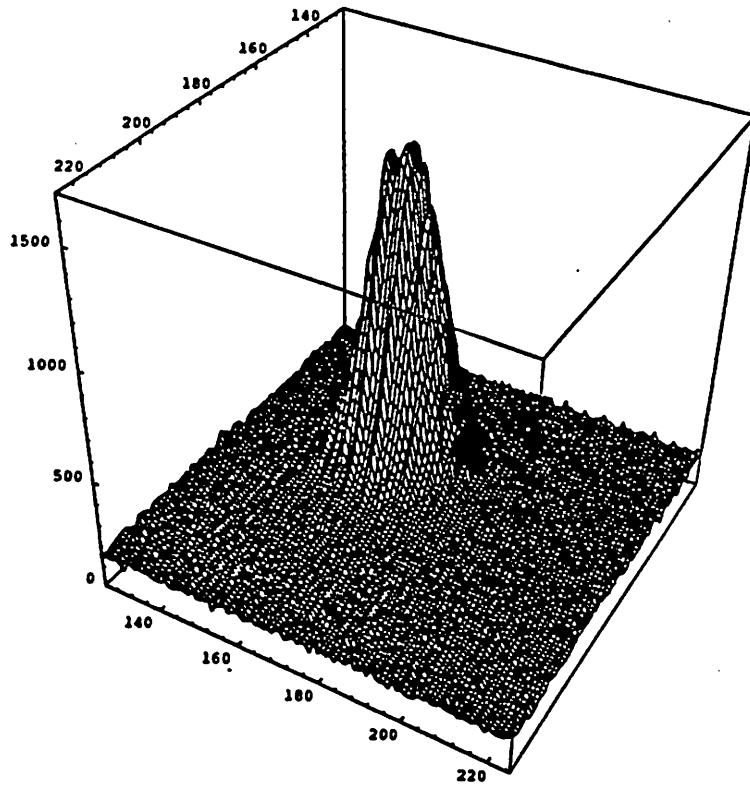


Figure 3.3  
Measured Aerial Image of 0.35 $\mu$ m Contact

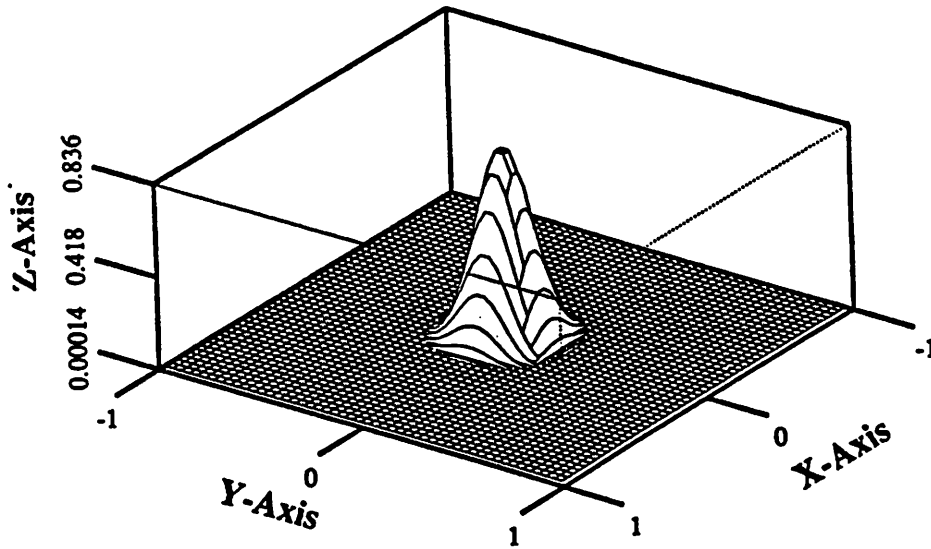


Figure 3.4  
Simulated Image of 0.35 $\mu$ m Contact

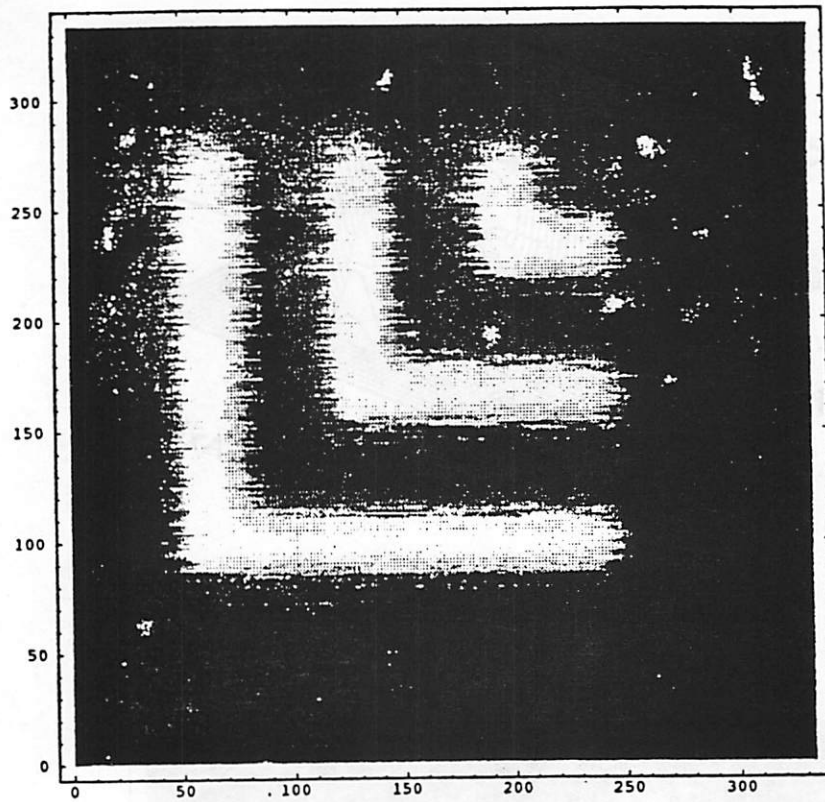


Figure 3.5  
Intensity Plot of  $0.5\mu\text{m}$  Elbow Array

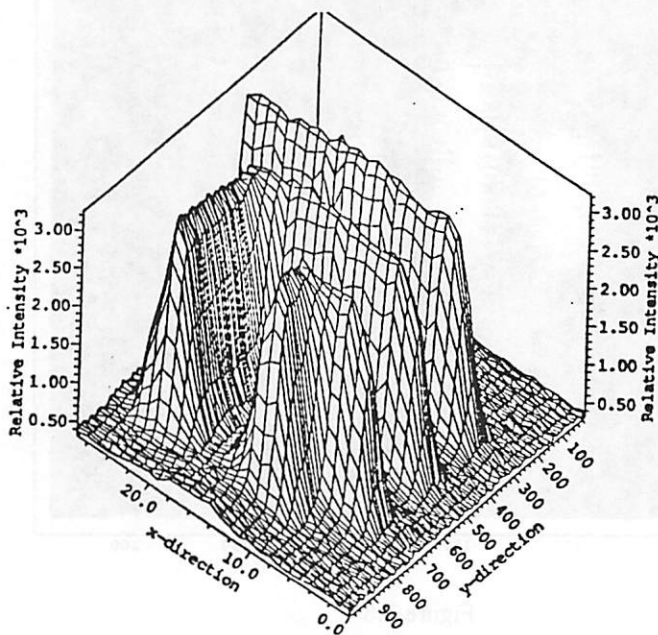


Figure 3.6  
Measured Aerial Image of  $0.5\mu\text{m}$  Elbow Array

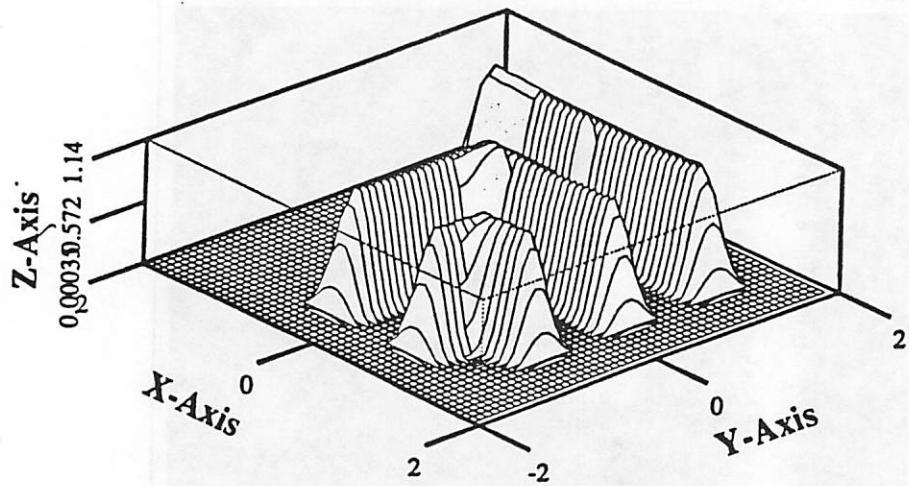


Figure 3.7  
 Simulated Image of 0.5μm Elbow Array Pattern

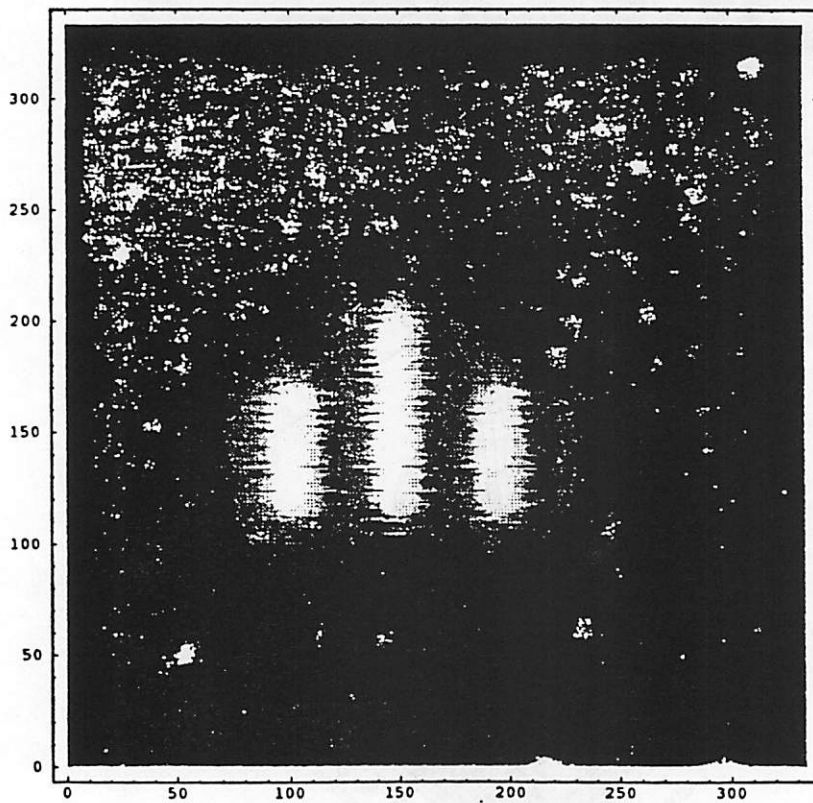


Figure 3.8  
 Intensity Plot of 0.35μm Isolated Line Pattern

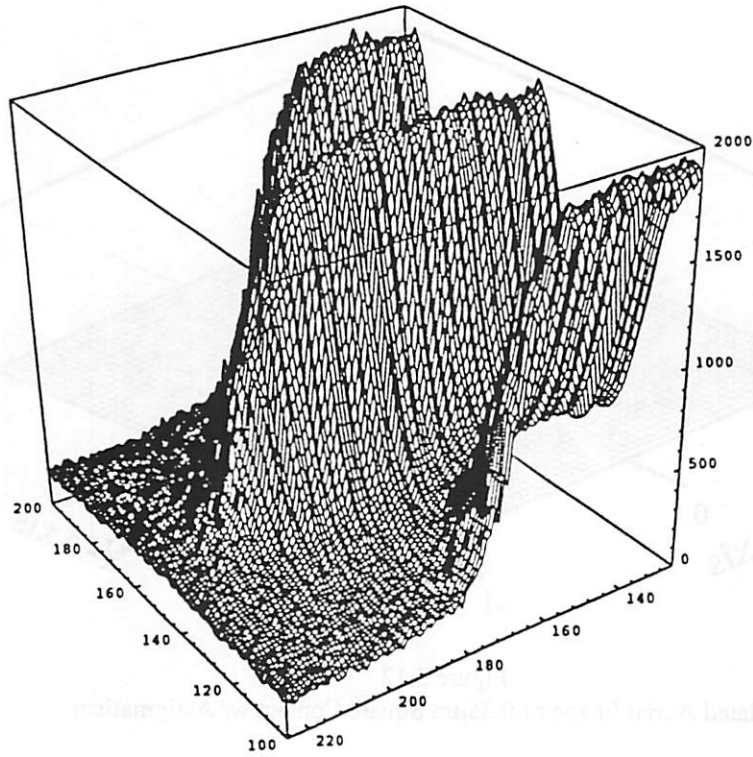


Figure 3.9  
Measured Aerial Image of 0.35 μm Isolated Line Pattern

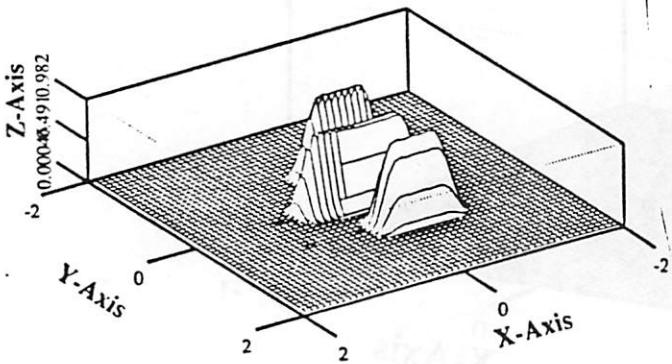


Figure 3.10  
0.0 μm defocus

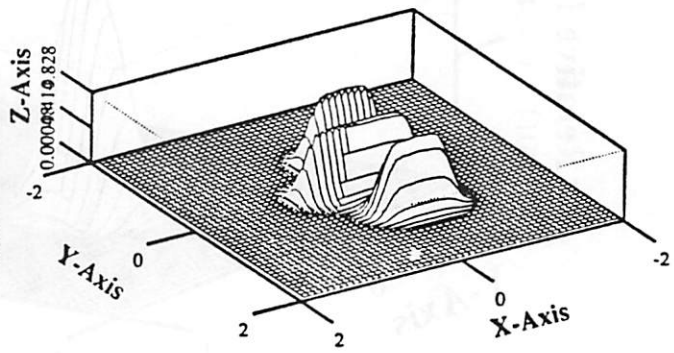


Figure 3.11  
0.5 μm defocus

Simulated Images of Isolated Line Pattern with varying defocus

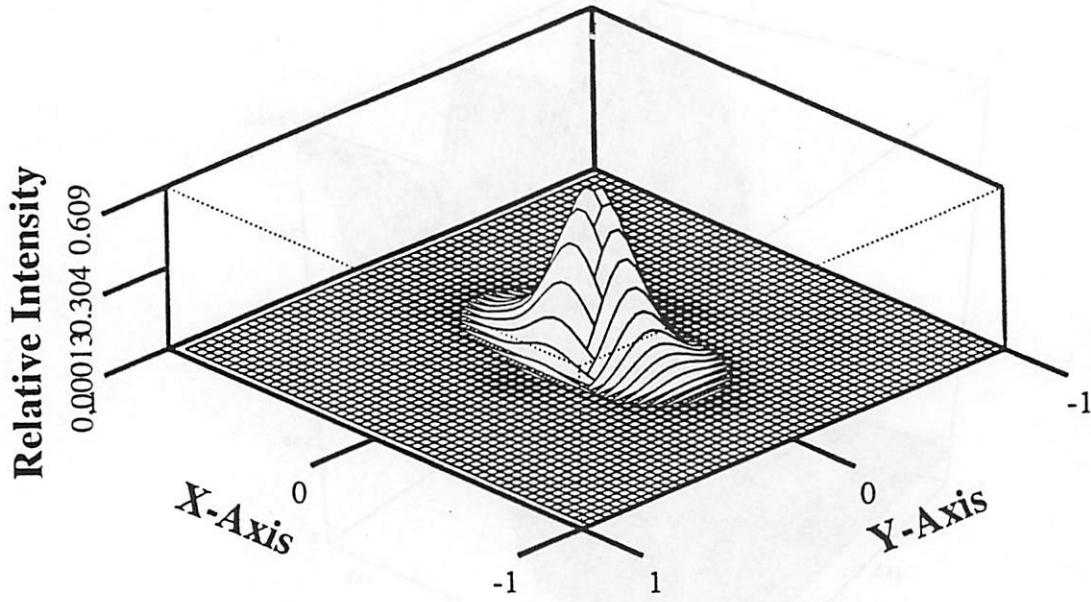


Figure 3.12  
 Simulated Aerial Image of  $0.35\mu\text{m}$  Square Contact w/ Astigmatism

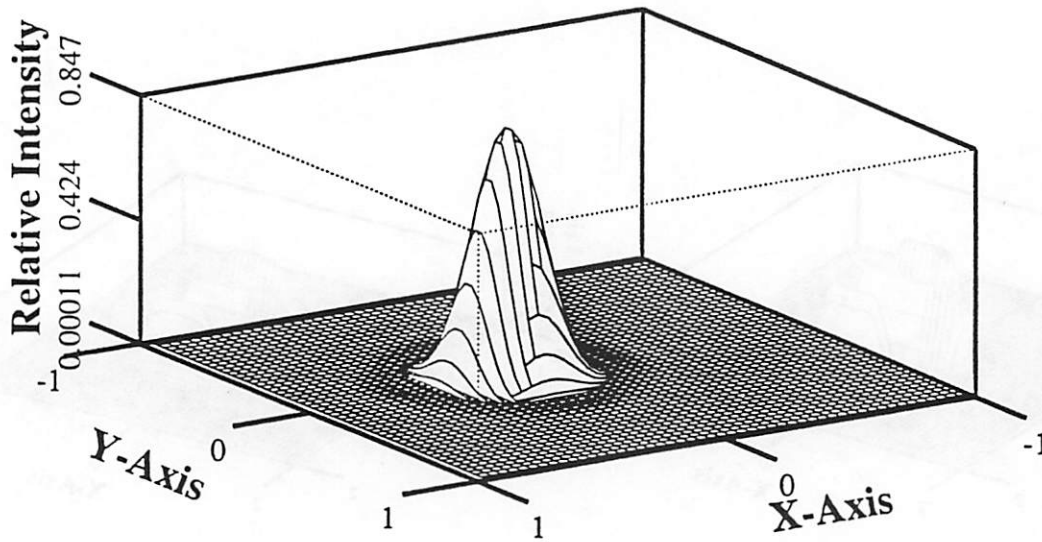


Figure 3.13  
 Simulated Aerial Image of  $0.35\mu\text{m}$  Square Contact w/ Distortion

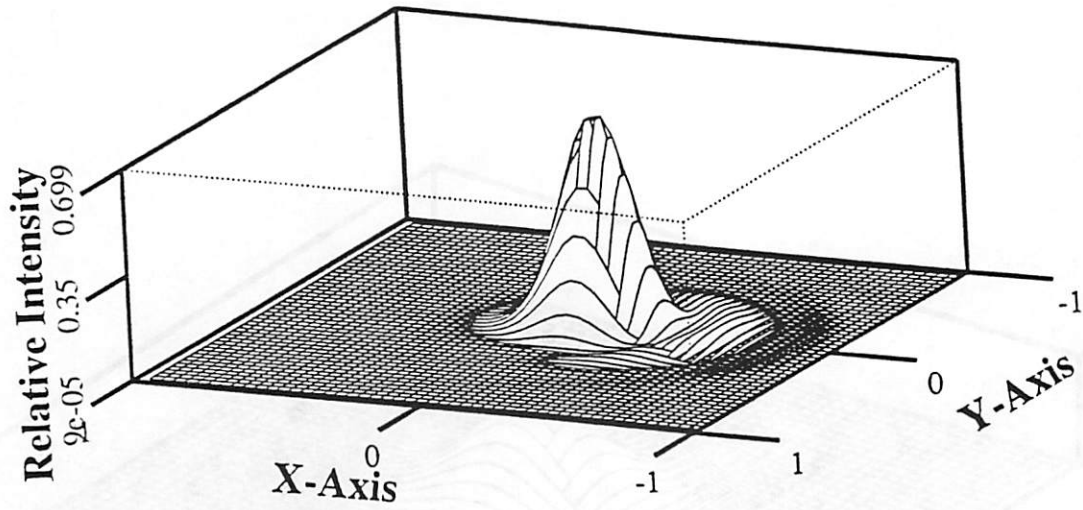


Figure 3.14  
 Simulated Aerial Image of  $0.35\mu\text{m}$  Square Contact w/ Coma

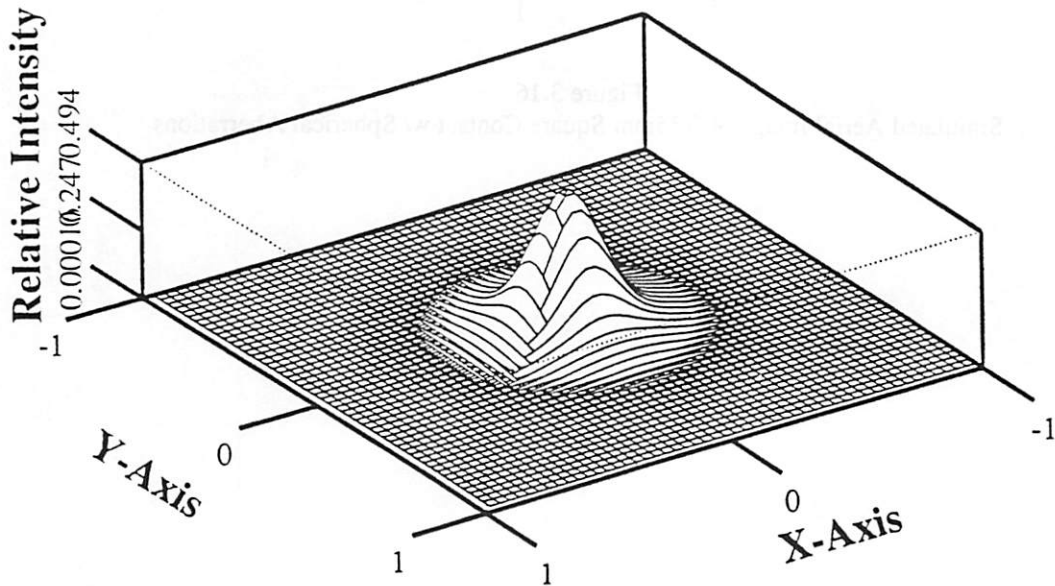


Figure 3.15  
 Simulated Aerial Image of  $0.35\mu\text{m}$  Square Contact w/ Curvature

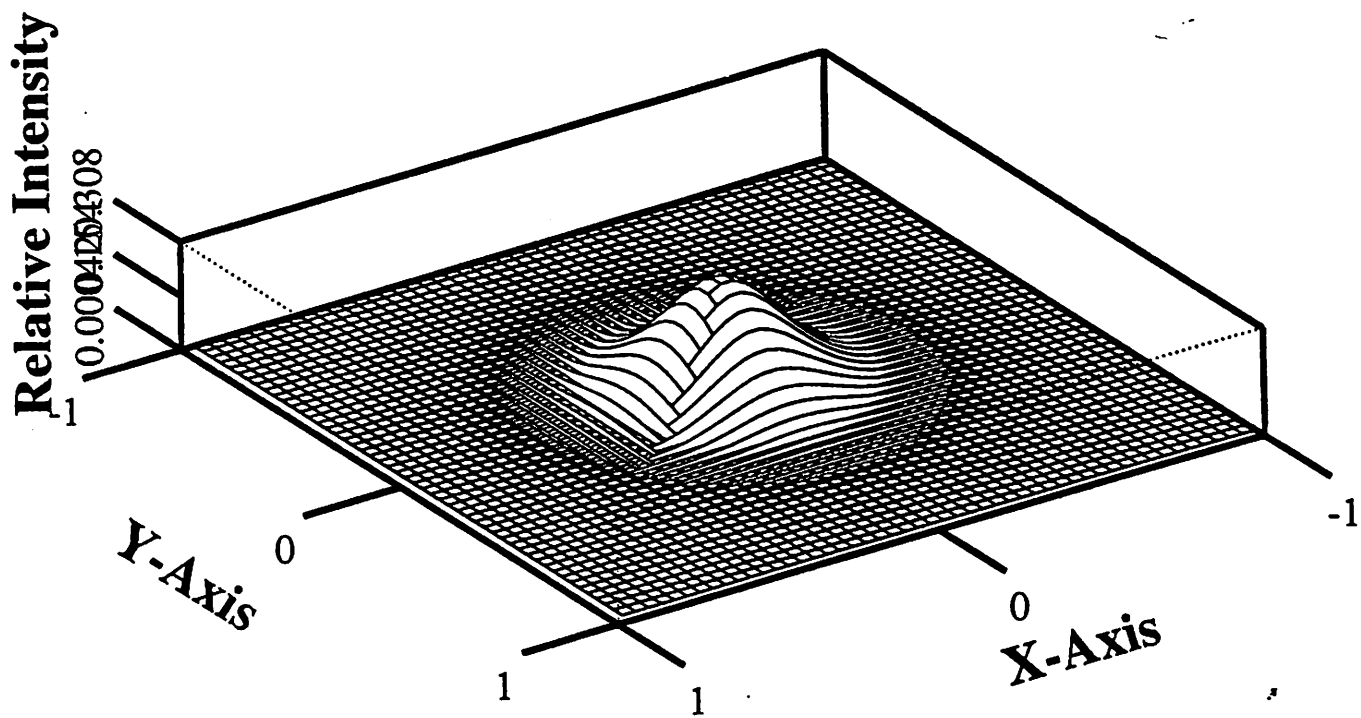


Figure 3.16  
Simulated Aerial Image of 0.35mm Square Contact w/ Spherical Aberrations

## References

1. Madan and Shaw, **The Physics and Applications of Amorphous Semiconductors** (Academic Press, Inc. 1988).
2. C.R. Wronski; *Solid State Technology*, p. 113 (June, 1988)
3. G. Lubberts and B. C. Burkey, *Journal of Applied Physics* 55 no. 3, p.760 (February 1, 1984).
4. R.E. Jones, Jr. and S.P. Wesolowski, *J. of Appl. Physics* 56 no 6, p1701 (September 15, 1984).
5. K. Tadros, A.R. Neureuther and R. Guerrieri, *Proc. SPIE* 1464-16 (1991)
6. C.R. Wronski, *Solid State Technology*, p.113 (June 1988)
7. T. D. Moustakas, *J. of Electronic Material*, vol. 8, p 391 (1979)
8. **Handbook of Optical Constants of Solids** Vols. I II, E.D. Palik Ed., Academic Press Inc. (1985).
9. B. Abeles, T. Tiedje; *Phys. Rev. Lett.*, vol. 51, p. 2003 (1983).
10. M. Hirose, S. Miyazaki; *J. Non-Cryst. Solids*, vol. 66, p. 327 (1984).
11. A. Pfau, M.S. Thesis, University of California Berkeley, 1991
12. W. Partlo, C. Fields, and W. Oldham, "Direct Aerial Image Measurement as a Method of Testing High Numerical Aperture Microlithographic Lenses," EIPB 93, San Diego June 4, 1993.
13. C. Fields, R. Bojko, and W. Oldham, "The Use of Amorphous Silicon for Deep UV Masks," *SPIE Proceedings*, March 1993.
14. C. Fields, W. Partlo, and W. Oldham, "Direct Aerial Image Measurements on a Commercial Stepper", TechCon'93 Conference, Atlanta Georgia, September 28-30, 1993.
15. T. Brunner, S. Cheng, and A. Norton, "A Stepper Image Monitor for Precise Setup and Characterization," *SPIE*, Vol. 922, pp.366-375, March 1988.